Effects of size and geometry on the plasticity of high strength copper/tantalum nanofilamentary conductors obtained by severe plastic deformation

Vanessa Vidal, Ludovic Thilly, Florence Lecouturier, Pierre-Olivier Renault

Effects of size and geometry on the plasticity of high-strength copper/tantalum nanofilamentary conductors obtained by severe plastic deformation

V. Vidal [a,b], L. Thilly [b,*], F. Lecouturier [a], P.-O. Renault [b]

[a] *Laboratoire National des Champs Magnétiques Pulsés, CNRS – Université Paul Sabatier Toulouse III – INSA, 143 Avenue de Rangueil, 31432 Toulouse, France*

[b] *Laboratoire de Métallurgie Physique, Université de Poitiers, SP2MI, Teleport 2, BP 30179, Bd M. et P. Curie, 86960 Futuroscope, France*

Abstract

Copper-based high-strength nanofilamentary wires reinforced by tantalum nanofilaments were prepared by severe plastic deformation (repeated hot extrusion and cold drawing steps) to be used in the windings of high-pulsed magnets. This application requires a complete characterization of the microstructure and the strength and their relationship for further optimization: after heavy strain, the Cu matrix is nanostructured and the Ta nanofilaments develop a strong ribbon-like shape resulting in an early microstructural refinement. The macroscopic strength is greater than rule-of-mixture predictions as confirmed by nanohardness values. The observed size effect is related to the dislocation starvation in the nanostructured materials combined with the barrier role of Cu/Ta interfaces. The strengthening is lower, however, as expected, because of the distorted ribbon morphology of the Ta filaments preventing them from behaving as nanowhiskers, as Nb fibers do in Cu/Nb wires. This shows that size and geometry play key roles in the plasticity of nanomaterials.

Keywords: Severe plastic deformation; Nanoindentation; TEM; Nanostructure; Fiber-reinforced composites

1. Introduction

The design and construction of non-destructive high-field magnets still represent a significant challenge for materials selection and development because the components have both structural (high elastic limit) and functional (high electrical conductivity) requirements that are usually contradictory. As an example, the production of fields above 80 T requires conducting materials possessing an electrical resistivity close to that of annealed copper (0.2 μΩ cm at 77 K) and a yield stress as high as possible (above 1.8 GPa at 77 K) to support the Lorentz forces without damage [1]. Up to now, reinforced copper-based wires have shown the best compromise between these two criteria; in particular, the copper/niobium (Cu/Nb) system has been studied for decades since it has very good mechanical properties that are much better than rule-of-mixture (ROM) predictions when the size of the Nb filaments is reduced to the sub-micrometer range. It should be emphasized that two main fabrication routes have been studied: production of nanofilamentary Cu/Nb wires via severe plastic deformation (SPD) of: (i) arc-melted Cu–Nb ingots, initially consisting of a Cu matrix containing Nb dendrites, so-called "in situ" composites; and (ii) bulk Cu tubes and Nb rods, giving rise to a Cu matrix containing Nb continuous filaments, so-called "continuous" composites [2–13].

The Laboratoire National des Champs Magnétiques Pulsés (Toulouse, France) has been involved in the improvement of these continuous composite materials for more than a decade: a fabrication process based on SPD through repeated extrusion, cold drawing and

* Corresponding author. Tel.:+33 5 49 49 68 31; fax: +33 5 49 49 66 92.
E-mail address: ludovic.thilly@univ-poitiers.fr (L. Thilly).

restacking steps has been developed. The best first generation of Cu/Nb "continuous" nanocomposite conductors were composed of a copper matrix containing $N = 55^4 = 9.15 \times 10^6$ parallel continuous Nb filaments with a diameter of 40 nm. At 77 K, they possess an ultimate tensile strength (UTS) of 2 GPa and a resistivity of 0.6 μΩ cm for a 0.04 mm^2 section [14]. However, conductors with a section between 3 and 7 mm^2 are required for use in pulsed magnets. Therefore, the effect of SPD on the microstructure as well as the influence of nanometer size on the plasticity of nanofilamentary Cu/Nb wires have been studied by in situ deformation using transmission electron microscopy (TEM), tomographic atomic probes, classic tensile tests and nanoindentation tests. The result is the definition of parameters for mechanical optimization (see Ref. [15] for a complete summary of these studies). Thus, a second generation of Cu/Nb wires containing $N = 85^4 = 52.2 \times 10^6$ parallel continuous Nb filaments were fabricated: the best nanofilamentary "continuous" conductor, containing Nb filaments with diameters of 142 nm, shows for a section of 5 mm^2 an UTS of 1.9 GPa and a resistivity of 0.58 μΩ cm at 77 K [16].

Studies of strengthening mechanisms have led to different ways of optimization. One is based on the following result: the strength of Nb nanofibers was observed to be inversely proportional to their diameter and approached, for the smallest diameters, the theoretical strength for perfect crystals, $\mu/2\pi$, where μ is the shear modulus; the Nb filaments can therefore be considered as nanowhiskers [13,17]. Since the shear modulus of tantalum (Ta) is higher than that of Nb ($\mu_{Ta} = 69$ GPa $> \mu_{Nb} = 40$ GPa), the Cu/Ta system is assumed to induce better mechanical properties. The same trend is expected using Fe as the reinforcing phase, since $\mu_{Fe} = 80$ GPa (in this case, however, poorer electrical properties are expected due to the miscibility between Cu and Fe at high temperatures). In the literature, numerous studies of heavily deformed composites which consist of a face-centered cubic (fcc) matrix and a body-centered cubic (bcc) reinforcing phase are reported: "in situ" Cu/Nb [2–12], Cu/Ta [18,19] and Cu/Fe [20,21] systems. They all illustrate the considerable interest in Cu-based fcc/bcc composites because of the good combination of conductivity and strength. In particular, the improved strength observed in "in situ" Cu/Ta nanocomposites compared to "in situ" Cu/Nb ones [18,19] seems to confirm that Cu/Ta wires exhibit better strengthening mechanisms. The crucial point is to understand the origin of such increased strength: does it derive from intrinsic properties of the Ta component (in the bulk state, Ta is harder than Nb) or from microstructural features such as geometry of the reinforcement or size effect on the composite plasticity (whisker effect in the Ta fibers or other dimensional dependence)?

In order to attempt to answer this question, we report here some recent developments of "continuous" Cu/Ta ultrahigh-strength conductors, and compare their properties to "continuous" Cu/Nb nanofilamentary wires.

Therefore, this paper reports on the complete characterization of different Cu/Ta samples taken throughout the fabrication process. The electrical resistivity was measured using the four-probe technique, while the microstructure was characterized using scanning electron microscopy (SEM), TEM and X-ray diffraction (XRD); the mechanical properties were investigated using macroscopic tensile tests, as well as nanoindentation. Particular care was taken to link the characterization results obtained at different length scales (micro-/macroscale).

2. Fabrication process of Cu/Ta nanofilamentary wires by SPD

As mentioned earlier, the Cu/Ta system was chosen for the higher value of shear modulus of Ta with respect to Nb. Its co-deformation behavior was initially investigated by cold drawing: radial and longitudinal oscillations were observed at the Cu/Ta interface leading to untimely fracture [22]. To prevent this phenomenon, a hot extrusion stage was added prior to the cold drawing process. The stress field is indeed simplified during extrusion since only section reduction occurs in the die; moreover, the high-temperature deformation induces a faster development of instabilities: after hot extrusion, only the radial undulations (i.e. the non-prejudicial ones) are developed and they attain an equilibrium state. During the subsequent cold drawing process, the Cu/Ta interfaces do not evolve further and early fractures are stopped.

Sophisticated "continuous" nanofilamentary Cu/Ta conductors were therefore fabricated via SPD applied by hot extrusion and cold drawing, together with bundling stages in order to reduce the fiber size. In the first stage a Ta rod was inserted in an oxygen-free high-conductivity (OFHC) Cu tube. The billet was processed by hot extrusion and cold drawn to a hexagonal shape. To reduce the filament size, the hexagonal composite wire was cut into 85 segments to be bundled into a can of OFHC Cu and reduced as in the first stage. The series of hot extrusion/cold drawing/bundling was repeated n times ($n \leqslant 4$) to obtain conductors containing $N = 85^n$ Ta nanofibers, resulting from a first optimization of engineering parameters [23]. Cu/Ta nanocomposites containing up to $N = 85^4$ Ta nanofibers were successfully fabricated. Theoretically, the filaments have a known distribution and bundles are separated by channels of pure Cu.

To illustrate the structure, a conductor, containing 85^3 Ta fibers and cold drawn down to a hexagonal shape ($h = 3.35$ mm) with one intermediate annealing, is presented in Fig. 1. Groups of 85 Ta fibers are observed, whereas the Cu matrix is distributed into the interfilamentary channels (Cu-0), the superfilamentary channels (Cu-1), etc.

Table 1 gives the theoretical dimensional properties of the Cu/Ta composites at different fabrication stages. The scale of the structure before and after drawing can be described using a similitude model, where the reduction

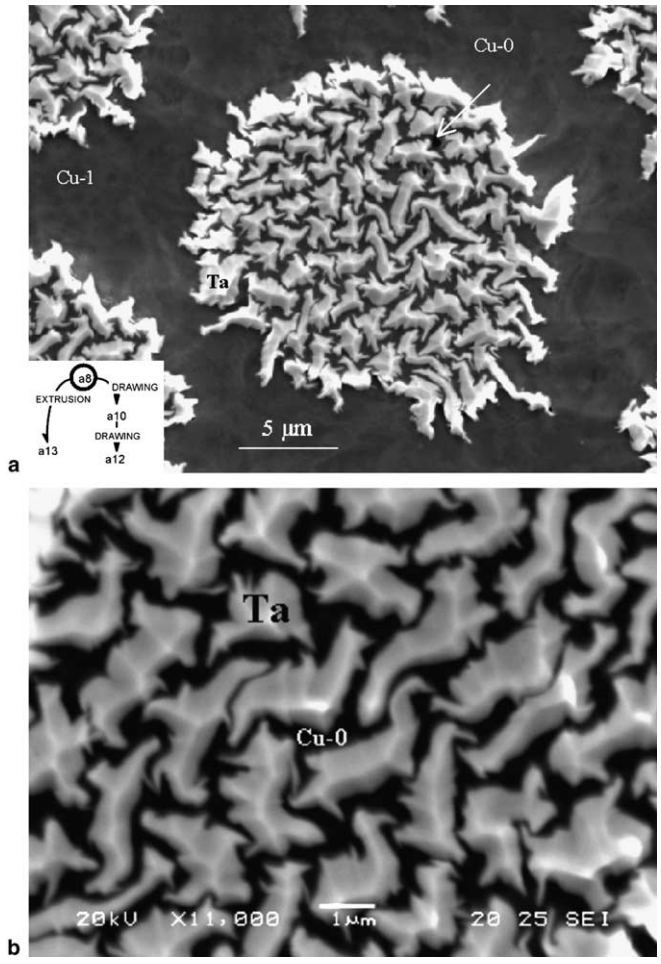

Fig. 1. (a) High-magnification cross-section SEM image of a Cu/Ta wire (sample a8: $N = 85^3$, $h = 3.35$ mm). (b) Close-up view of the Ta + Cu-0 region.

of the scale of the structure is proportional to the strain. The total logarithmic true strain or drawing ratio (η) is given by $\eta = \ln(A_0/A)$, where A is the section of the wire and A_0 is the initial section of the billet. The reduction in area (RA) is also defined as $\mathrm{RA} = (A_i - A)/A_i$, where A_i is the section of the wire at the previous recrystallization annealing stage. It is worth mentioning that after each bundling stage into a new Cu can, the total Ta volume fraction (% Ta) decreases from 66.2% at $N = 1$ down to 7.5% at $N = 85^4$.

3. Microstructural characterization

3.1. Texture analysis

The development of the macroscopic texture during the repeated hot extrusion and cold drawing stages was first studied using XRD measurements. The local texture of Cu and Ta was also investigated using TEM selected area electron diffraction (TEM SAED) as discussed in Section 3.2.

XRD patterns were obtained using a Seifert diffractometer. The texture developed in the drawing axis direction was characterized by standard θ–2θ scans using Cu Kα radiation. θ–2θ scans were obtained from cross-sections of specimens taken throughout the fabrication stages.

A useful way to characterize the formation of fiber textures is to compute the integrated intensities of the Bragg peaks from θ–2θ scans and to compare them to each other in terms of the ratio of the integrated intensity $I(h\,k\,l)$ of the $(h\,k\,l)$ peaks to the integrated intensity of the dominant peak: in our case $I(h\,k\,l)/I(1\,1\,0)$ for Ta and $I(h\,k\,l)/\mathrm{I}(1\,1\,1)$ for Cu. Figs. 2(a) and (b) show the evolution of the texture in the Ta fibers and in the Cu matrix during processing at each stage, after hot extrusion and after heavy drawing, using the most significant Bragg peaks. In addition, data for annealed polycrystalline materials (standard Ta and standard Cu) are added to these plots for comparison.

For the Ta fibers (Fig. 2(a)), we notice that from the first stage and throughout the fabrication process, the integrated intensities of the $(2\,0\,0)_{\mathrm{Ta}}$ and $(2\,1\,1)_{\mathrm{Ta}}$ diffraction

Table 1
Dimensional characteristics of a selection of Cu/Ta conductors

Sample	N	d (mm)	%Ta	d_{Ta} (nm)	$d_{\mathrm{Cu\text{-}0}}$ (nm)	$d_{\mathrm{Cu\text{-}1}}$ (μm)	$d_{\mathrm{Cu\text{-}2}}$ (μm)	$d_{\mathrm{Cu\text{-}3}}$ (μm)	$d_{\mathrm{Cu\text{-}4}}$ (mm)	RA (%)	η
a1	1	15	66.2	1.22×10^7	1.4×10^6	–	–	–	–	≈ 0 (E)	2.1
a2		3.35*	66.2	2.86×10^6	6.53×10^5	4000	–	–	–	99.3	5
a3	85	18	41.5	1.2×10^6	2.73×10^5	1670	–	–	–	≈ 0 (E)	6.7
a4		3.35*	41.5	2.33×10^5	5.3×10^4	653	4000	–	–	99.3	10
a5	85^2	18	23.4	9.7×10^4	2.2×10^4	273	1670	–	–	≈ 0 (E)	11.8
a6		3.35*	23.4	1.9×10^4	4350	53	653	4000	–	99.3	15
a7	85^3	18	13.2	7.97×10^4	1820	22	273	1670	–	≈ 0 (E)	16.8
a8		3.35*	13.2	1550	355	4	53	653	–	88.2	20
a9		2.41	13.2	1060	244	2.99	36.6	224	–	94.4	20.8
a10		1.83	13.2	810	185	2.27	27	170	–	96.69	21.3
a11		1.398	13.2	619	144	1.76	21.6	130	–	98.13	21.9
a12		1.293	13.2	572	131	1.6	19.6	120	–	98.4	22
a13	85^4	18	7.5	650	149	1.82	22.3	273	1.40	≈ 0 (E)	21.8

N, filament number; d, wire total diameter (*hexagonal section); %Ta, total Ta volume fraction; d_{Ta}, theoretical Ta filament diameter; $d_{\mathrm{Cu\text{-}}i}$, theoretical width of Cu-i channel; RA, reduction in area (see text); E, sample taken after hot extrusion; η, total logarithmic true strain (see text).

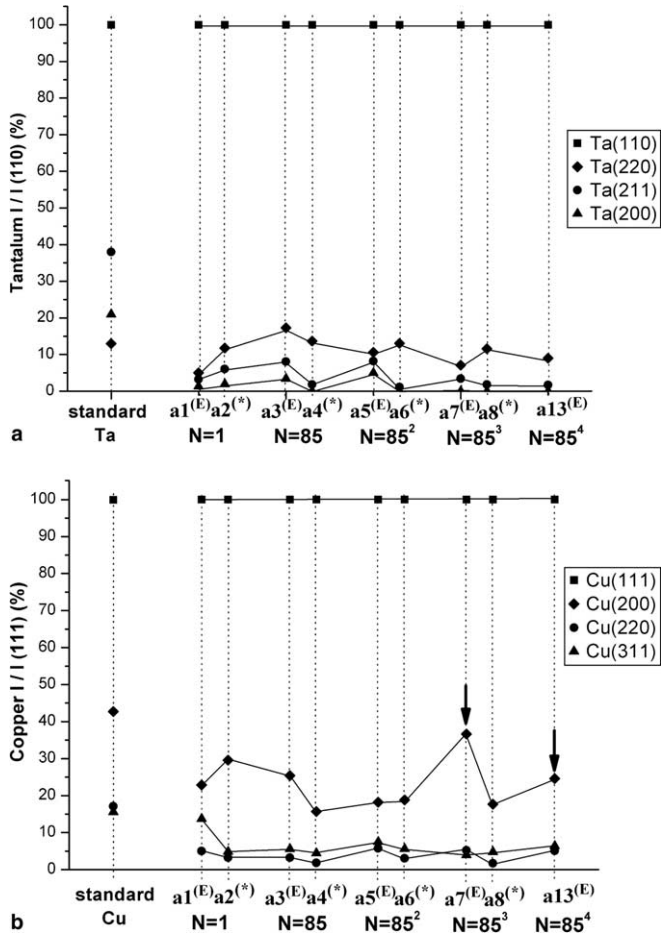

Fig. 2. Ratio of integrated intensities of the Bragg peaks from θ–2θ XRD scans on Cu/Ta nanofilamentary wires at different fabrication stages (hot extruded or heavily cold drawn). Development of texture appears: (a) in Ta and (b) in Cu (solid lines are guides to the eyes) (*hexagonal section; E, sample taken after hot extrusion).

peaks markedly decrease and the integrated intensities of the $(1\,1\,0)_{Ta}$ and $(2\,2\,0)_{Ta}$ peaks remain strong. This confirms that Ta develops a strong $\langle 1\,1\,0\rangle$ fiber texture parallel to the wire axis during the fabrication process as reported in the literature for heavily drawn bcc metals [24]. In particular, the same result was obtained with drawn Cu/Nb nanofilamentary wires [25].

For the Cu matrix (Fig. 2(b)), the ratio of the integrated intensities of the $(2\,0\,0)_{Cu}$ to $(1\,1\,1)_{Cu}$ diffraction peaks noticeably increase for the a7 and a13 samples after hot extrusion (data points marked with an arrow). Several θ–2θ scans were carried out and confirmed this result. Therefore, Cu exhibits two texture components along the wire axis: a major $\langle 1\,1\,1\rangle$ component and a $\langle 2\,0\,0\rangle$ component which remains significant throughout the fabrication process.

It is usually observed that the $\langle 2\,0\,0\rangle$ component in fcc metals tends to disappear during drawing leading to a single $\langle 1\,1\,1\rangle$ texture in heavily drawn fcc metals [24]. This was indeed observed during the fabrication process of Cu/Nb nanofilamentary wires [25] but not during the fabrication of Cu/Ta nanofilamentary wires studied in the present paper. However, it was recently reported that the major $\langle 1\,1\,1\rangle$ and the minor $\langle 2\,0\,0\rangle$ components, developed as a duplex texture in axisymmetrically deformed fcc metals, change to strong $\langle 2\,0\,0\rangle$ components after recrystallization heat treatments [10,26]. It is worth mentioning that after each bundling stage, the Cu/Ta conductors are hot extruded after annealing at 700 °C: the Cu matrix is then fully recrystallized. Therefore, the origin of the rather strong $\langle 2\,0\,0\rangle$ texture could be explained by the annealing and hot extrusion stages. As suggested in Ref. [26] according to the strain energy release maximization model, the $\langle 2\,0\,0\rangle$ oriented grains might retain their texture while the $\langle 1\,1\,1\rangle$ grains tend to the $\langle 2\,0\,0\rangle$ orientation via high-angle boundary migration. However, it appears important to study thoroughly the texture development during the elaboration of the Cu/Ta nanofilamentary wires, since there is no clear correlation between the fraction of the $\langle 2\,0\,0\rangle$ component and the strain state of the conductors. To do so, complete pole figures should be obtained.

In summary, this study revealed that Ta develops a $\langle 1\,1\,0\rangle$ texture parallel to the wire axis while Cu exhibits a duplex texture with a $\langle 1\,1\,1\rangle$ major orientation and a secondary $\langle 2\,0\,0\rangle$ component along the wire axis, which is not observed in the Cu/Nb system.

3.2. Microstructure analysis

3.2.1. Sample preparation

TEM specimens were prepared by mechanical polishing to a thickness of 80 μm followed by a tripod-polishing step. Then, samples were argon ion milled with a Gatan Model dual-gun ion mill at liquid-nitrogen temperature using an accelerating voltage of 5 kV and a 14° tilt.

3.2.2. General results

TEM observations were carried out using a JEOL 200CX instrument operating at 200 kV. Figs. 3–5 present the microstructures of a10, a12 and a13 samples for both transverse and longitudinal sections. In bright-field images, Ta appears darker than Cu. This is explained by the fact that Ta is a much heavier element. Moreover, due to the difference in hardness between Cu and Ta, the Cu regions are thinner than the Ta regions.

On the transverse section, the Ta fibers appear flattened and curled (Figs. 3(a–c), 4(a) and (b) and 5(a)) containing nanograins with sizes ranging from 100 to 200 nm (Figs. 3(c) and 5(b)) which is similar to the size of dislocation cells observed in heavily cold worked Nb. These nanograins are thus due to the transformation of cell walls into subgrain boundaries then into grain boundaries during intensive plastic deformation ($\eta > 20$) as a result of dynamic recrystallization coupled to static recovery during intermediate annealing.

Because of the multiscale structure, different sizes of Cu channels exist in Cu/Ta wires. In the largest Cu channels (Figs. 3(d) and (e) and 4(c)), grains both in micrometer

and in nanometer (200–400 nm) ranges are elongated along the drawing direction and have a high dislocation density. Dislocation substructures are shown in Figs. 3(d) and 4(c). These types of cells with dislocation walls and low internal dislocation density are characteristics of heavily deformed metals.

Fig. 3(e) shows two different SAED patterns from a same channel of Cu: as was observed in the XRD investigation, the Cu exhibits both $\langle 1\ 1\ 1\rangle$ and $\langle 2\ 0\ 0\rangle$ texture components. However, determination of a clear correlation between the size of Cu grains and this duplex texture was not possible by TEM observations.

The finest Cu channels are composed of single grains elongated along the drawing axis with their grain boundary perpendicular to the wire axis as indicated by arrows in Figs. 3(f) and (g). These Cu grains are longer than 3 μm.

In Fig. 4(b), the indexed SAED pattern from a Ta + Cu-0 zone shows the presence of a strong $\langle 1\ 1\ 0\rangle_{Ta}$ texture component for the Ta and characterizes the texture of the interfilamentary Cu-0 as composed of $\langle 1\ 1\ 1\rangle_{Cu}$ and $\langle 2\ 0\ 0\rangle_{Cu}$ components but also of a $\langle 2\ 2\ 0\rangle_{Cu}$ component ($\{1\ 1\ 1\}_{Cu}$ reflections), although it is considered as a weak orientation from the XRD study.

The presence of these three Cu texture components ($\langle 1\ 1\ 1\rangle$, $\langle 2\ 0\ 0\rangle$ and $\langle 2\ 2\ 0\rangle$) in this disturbed area, characterized by interfolded Ta ribbons, seems to show that the Ta constrains the Cu matrix in such a way that it essentially deforms to ensure the deformation compatibility with Ta without regard to its usual texture development.

Because of the highly irregular section of the Ta fibers, on longitudinal micrographs the same fiber can be seen as split into several strips, all parallel to the drawing direction. Thus, the deduction of the size of Cu must be done carefully from measurements of longitudinal micrographs.

Nevertheless, the width of the distinctive Cu channels is generally in good agreement with the theoretical dimensions listed in Table 1.

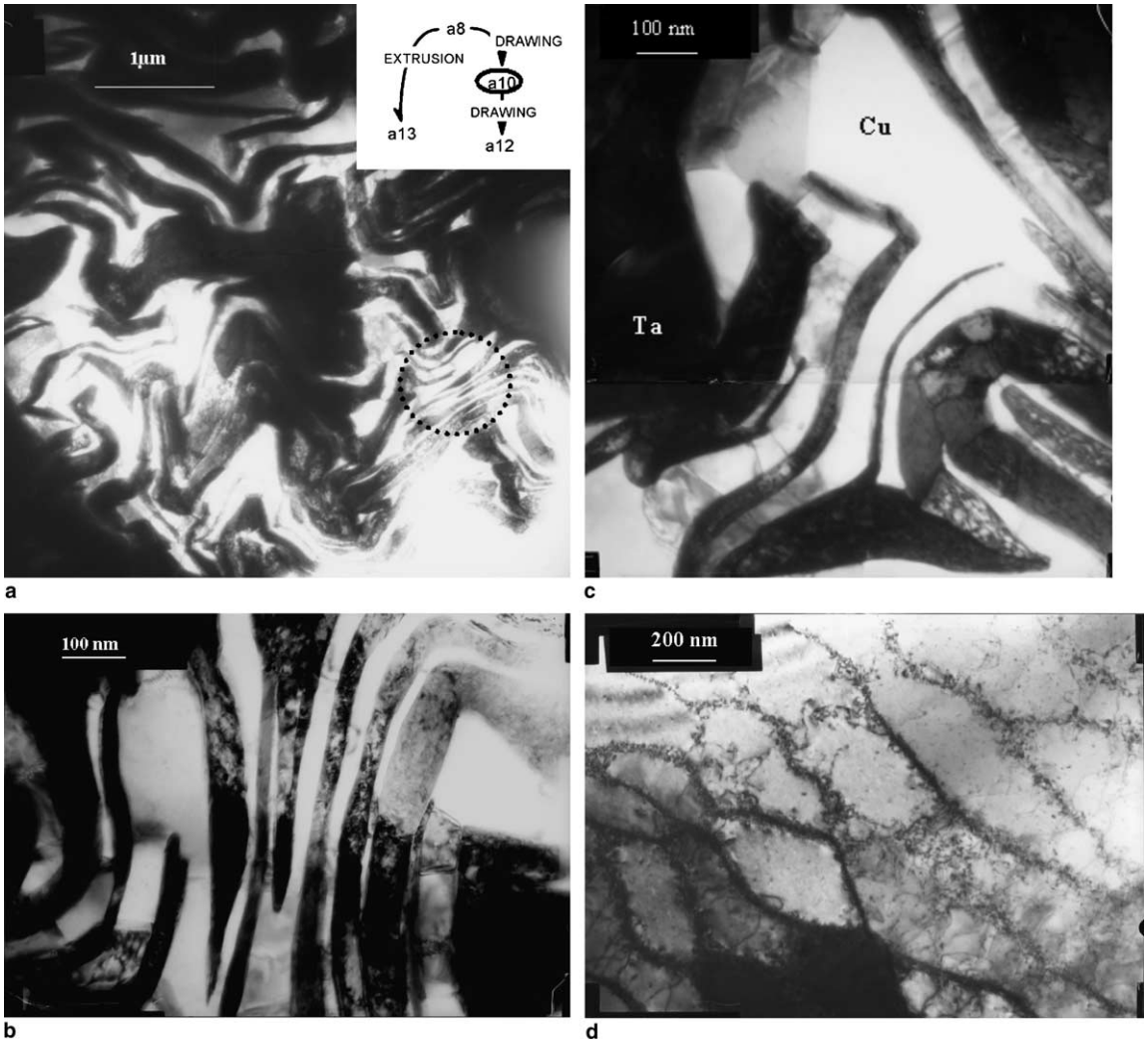

Fig. 3. Bright-field TEM images of a10 specimen ($N = 85^3$, $d = 1.8$ mm). Transverse section: (a) ribbon-like shape of the Ta filaments; (b) close-up of the dotted circle in (a); (c) grains in Ta fibres; (d) dislocation cell structure in Cu; (e) SAED patterns of a Cu-1 channel: $\langle 2\ 0\ 0\rangle$ above and $\langle 1\ 1\ 1\rangle$ below. Longitudinal section: (f) Cu channels composed of successions of single grains; (g) example of transverse grain boundary.

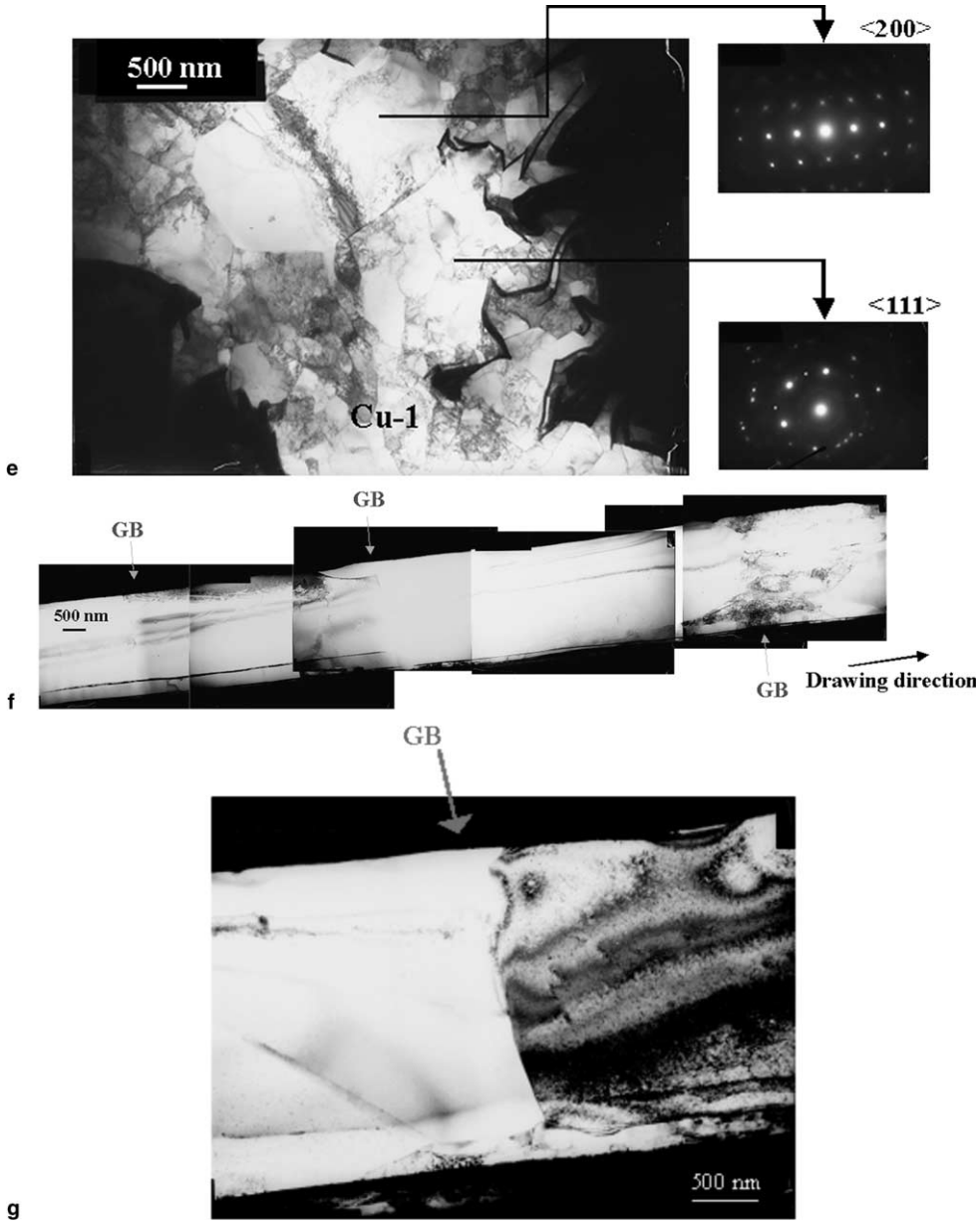

Fig. 3 (*continued*)

3.2.3. Geometry of the fibers

The observed ribbon-like structure of the Ta filaments (Figs. 1, 3(a–c), 4(a) and (b) and 5(a)) is characteristic of the bcc deformation mode when heavily drawn [24]. Bcc crystals with ⟨1 1 0⟩ drawing texture have slip systems orientated in such a way that plane-strain deformation is energetically more favorable than axisymmetric deformation (only two of the four ⟨1 1 1⟩ directions are orientated favorably to accommodate extension parallel to the fiber axis). Consequently, the fibers develop elliptical cross-sections normal to the wire axis resulting in the ribbon-like shape.

Such a shape was also observed for Nb fibers in Cu/Nb nanofilamentary wires but to a lesser extent. This could be due to the larger difference in the mechanical behavior between Cu and Ta, where the hard Ta is surrounded by softer Cu and hence is "free" to deform in the more energetically favorable configuration. The result is a rather inhomogeneous distribution in the Ta size. Similar microstructures are observed in heavily drawn "in situ" Cu/Fe composites, where Cu and Fe have also very different shear moduli [20,21] (it must be stressed here that even in "in situ" Cu/Nb composites rather strong curling is observed, resulting from the initial heterogeneous dendritic structure; this is not the case in the "continuous" Cu/Nb system, with an initial homogeneous filamentary structure).

Consequently, the definition of a diameter value becomes problematic. SEM and TEM images from cross-sections of samples a8, a10, a12 and a13 were examined to obtain reliable values for the microstructural dimensions: the results of the estimation of the effective filament

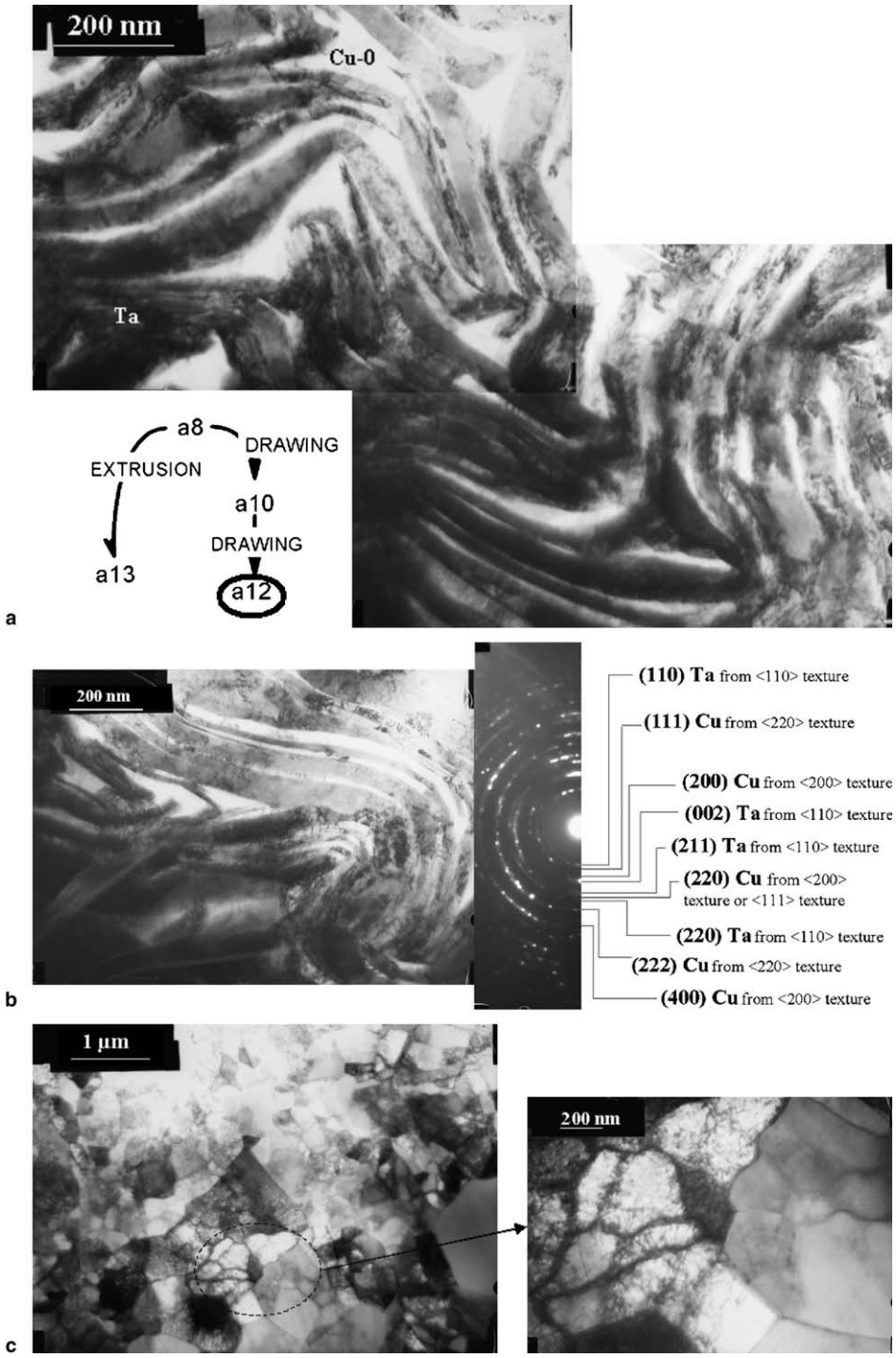

Fig. 4. Bright-field TEM images of transverse section from specimen a12 ($N = 85^3$, $d = 1.293$ mm). (a) Ribbon-like shape of the Ta filaments; (b) close-up of Ta ribbons + Cu-0 zones and associated SAED pattern; (c) different grain size in a large Cu channel and close-up of dislocation cell structure.

thickness, $t_{\mathrm{eff\,Ta}}$, are summarized in Table 2. As the dispersion of $t_{\mathrm{eff\,Ta}}$ is different for each sample, an average value is defined for small-dispersion samples (a8, a12 and a13). When the dispersion is too wide (sample a10), the average value has no microstructural sense, thus $t_{\mathrm{eff\,Ta}}$ is not defined. The filament evolution characterized by the effective thickness (replacing the theoretical Ta diameter) will be taken into account in the following sections.

Fig. 6 shows the microstructural evolution during hot extrusion and cold drawing by plotting the effective thickness (and its dispersion) versus the theoretical Ta diameter. During hot extrusion (conductor a8 to conductor a13), where a large strain is applied through only one deformation step, the thickness of the Ta ribbons and its dispersion reduces in a rather homogeneous manner. In contrast, after repeated cold drawing steps (8 passes between samples a8

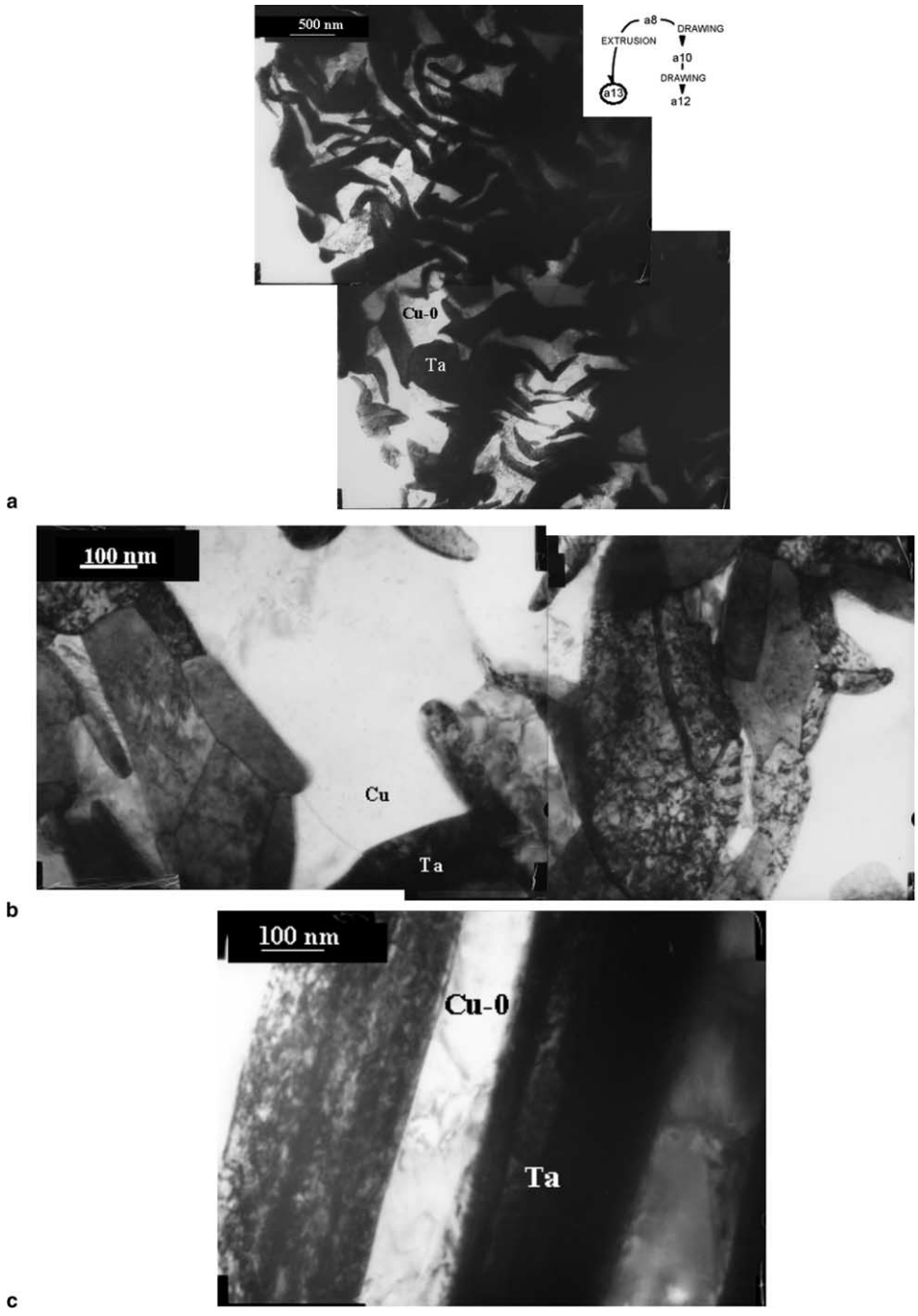

Fig. 5. Bright-field TEM images of (a,b) transverse and (c) longitudinal sections from specimen a13 ($N = 85^4$ after hot extrusion) showing Ta fibres surrounded by Cu.

and a10, 5 passes between samples a10 and a12), the reduction of the Ta dimension does not follow the same trend: the dispersion in ribbon thickness becomes very large for the a10 sample, while, after significant amount of strain (sample a12), the Ta ribbons flatten and rotate in transverse directions and the degree of microstructural refinement increases with a fairly small spread of values. This is evidence that the so-called ''curling'' phenomenon is induced by the repeated activation of only a few slip systems in the Ta fibers associated with repeated rotation and folding of the Ta + Cu-0 zones. Such a phenomenon mainly occurs during multiple drawing steps but does not have time to develop during single-step extrusion.

It is also interesting to note that samples a10 and a12 have the same lower bound thickness value showing a stabilization of the ribbon thickness at about 20 nm; this value could be considered as a critical Ta thickness corresponding to a plastic deformation limit as already observed during the drawing of Cu/Fe in situ composites [20]. This limit could be associated with the occurrence of internal

Table 2
Estimation of the effective Ta thickness observed for a selection of Cu/Ta conductors

	N	Size of the conductor (mm)	Observation technique	Theoretical Ta diameter d_{Ta}	Range of measured Ta thickness values	Effective Ta thickness (average) t_{effTa} (nm)
a8	85^3	$h = 3.35$	SEM	1.55 μm	[430 nm–1.14 μm]	812
a10	85^3	$d = 1.83$	TEM	810 nm	[24 nm–820 nm]	Not accurate
a12	85^3	$d = 1.293$	TEM	572 nm	[21 nm–145 nm]	72
a13	85^4	$d = 18$	TEM	650 nm	[92 nm–461 nm]	253

h, hexagonal section.

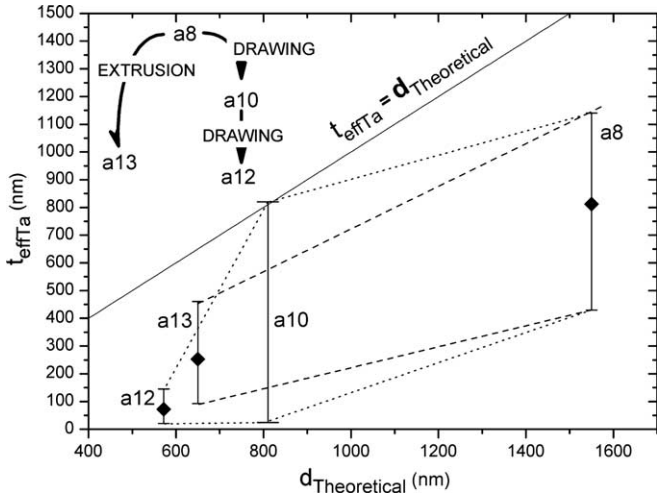

Fig. 6. Effective thickness, t_{effTa} (and its dispersion) versus the theoretical Ta diameter d_{Ta}. Differences of microstructural evolution during hot extrusion (dashed line) and drawing (dotted line) are observed (see text).

fractures during the final drawing stages that prevent one from obtaining samples finer than sample a12. In addition, the space restriction characterized by very narrow interfilamentary distances makes the co-deformation of the ribbons and the matrix more difficult, as observed in Figs. 4(a) and (b) (sample a12) where Cu-0 islands were formed (100 nm in size). Therefore, the elongation during drawing of the very fine-diameter conductors seems to be accommodated by the Cu matrix, through complex deformation (plasticity and grain boundary sliding) rather than true co-deformation of the system.

4. Electrical characterization

The electrical resistivity of Cu/Ta conductors was measured using the classic four-probe technique with a maximum current of 100 mA to avoid heating of the wires. The resistivity values for samples a9 ($d = 2.41$ mm), a10 ($d = 1.83$ mm) and a11 ($d = 1.398$ mm) at 77 K are, respectively, 0.375, 0.382 and 0.401 μΩ cm. The decrease of the electrical conductivity with a reduction in diameter results from the increase of dislocation density, the dislocations being scattering centers for electrons, and also from the size reduction of the finest Cu channels the thickness of which becomes comparable to the mean free path of electrons at 77 K (~ 200 nm). Since these channels become poor conductors, most of the current is transported in the outer Cu channels. Nevertheless, the resistivity remains smaller than twice that of annealed Cu (0.2 μΩ cm) and therefore satisfies the requirements for magnet applications.

5. Mechanical characterization

5.1. Experimental procedure

This section describes the mechanical testing of the Cu/Ta wires via macroscopic tensile tests as well as a nanoindentation study of the local mechanical properties with the indentation axis parallel to the filament axis. Segments of the nanocomposite conductors were cut using a metallographic saw and embedded in epoxy resin so that the cross-sectional surface of the wire can be perfectly perpendicular to the indenter axis. The samples were then mechanically polished. Nanoindentation experiments were performed using a nanohardness tester (CSM Instruments, SA) with a diamond Berkovich indenter (three-sided pyramid). A maximum load of 5 mN was applied with loading and unloading rates of 10 mN/min and a holding time of 10 s at maximum load. Hardness was determined from indentation load–displacement data using the Oliver–Pharr method [27].

A wide range of data for each phase was obtained: from the largest Cu-4 channels to the nanocomposite regions (here "nanocomposite regions" refers to the nanostructured multiphase regions).

5.2. Results

Different samples from the Cu/Ta system were tested and compared to the Cu/Nb system tested in previous studies [15]. Table 3 presents the characteristics of the Cu/Ta and Cu/Nb nanofilamentary wires and the average hardness H measured in the nanocomposite regions. The indents in these regions cover Ta + Cu-0 or Nb + Cu-0 according to the system tested. X_{nTa}, X_{nNb} and X_{nCu} are therefore the local volume fractions of Ta, Nb or Cu in the indented zones.

The mechanical properties of the individual phases in the Cu/Ta nanostructured conductors are illustrated in Fig. 7(a), which shows, in a log–log plot, the evolution of the hardness H of the tested zones versus the phase dimension d_α. The size parameter d_α corresponds to the

Table 3
Dimension, hardness data and deviation from ROM values of nanocomposite zones tested in Cu/Ta and Cu/Nb conductors

		N	d (mm)	d_{Ta} or d_{Nb} (nm)	$t_{eff\,Ta}$ (nm)	$d_{Cu\text{-}0}$ (nm)	Indented regions	X_{nTa} or X_{nNb}	X_{nCu}	H (MPa)	$H_{n\text{-}ROM}$ (MPa)	$\Delta H_{n\text{-}ROM}$ (%)
Cu/Ta	a8	85^3	3.35	1540	812	350	Cu-0 + Ta	0.66	0.34	4507	4312	+4.5
	a9	85^3	2.41	1060	–	240				4550		+5.5
	a10	85^3	1.83	810	–	180				4660		+8.1
	a11	85^3	1.398	619	–	144				5189		+20.3
	a12	85^3	1.293	572	72	131				5276		+22.4
	a13	85^4	18	643	252	140				4017		−6.8
Cu/Nb	b1	85^3	3.7	2200	–	670	Cu-0 + Nb	0.59	0.41	3104	3380	−8
	b2	85^4	3.3	186	–	560				5179		+53.2

X_α, local volume fraction of α phase; H, averaged nanohardness value; $H_{n\text{-}ROM}$, hardness from the nano-ROM (see text); $\Delta H_{n\text{-}ROM}$, deviation from n-ROM (see text).

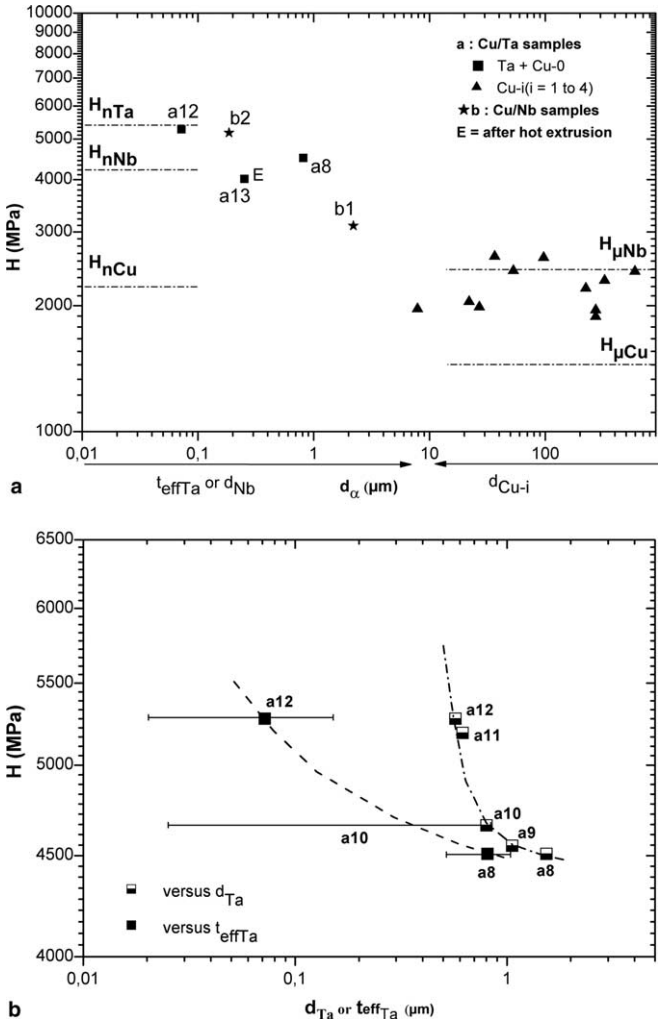

Fig. 7. (a) Hardness evolution versus d_α for Cu/Ta samples compared with Cu/Nb samples. α is the Cu-i ($i = 1$–4) phase in the micrometer range; α is the Ta or Nb phase for the indented nanocomposite regions. Note that for Cu/Ta, d_α is the "effective" size of the Ta ribbons (see text). H_α = hardness literature data of α phase, in bulk coarse-grain ($H_{\mu\alpha}$) or bulk nanostructured ($H_{n\alpha}$) states. (b) Hardness evolution of Cu/Ta samples versus both the theoretical Ta diameter (⬓) and the "effective" size of the Ta ribbons (■). Dashed and dash–dot lines are guides for the eye.

channel width of the Cu-i phase ($i = 1$–4) in the micrometer range while for the indented nanocomposite regions d_α corresponds to the previously defined effective Ta filament thickness, $t_{eff\,Ta}$, or to the Nb filament diameter d_{Nb}. The hardness data of the nanocomposite regions in the Cu/Nb system have been included (values in Table 2). The literature hardness data for bulk cold drawn coarse-grain Nb and Cu as well as for bulk nanocrystalline Nb and Cu have been included in the plot ($H_{\mu Nb} = 2.4$ GPa, $H_{\mu Cu} = 1.6$ GPa and $H_{nNb} = 4.2$ GPa, $H_{nCu} = 2.2$ GPa, respectively). Fig. 7(b) illustrates the effect of the early refinement of the Ta ribbons on the mechanical properties by plotting the hardness evolution in the nanocomposite zones in Cu/Ta samples versus both the theoretical diameter d_{Ta} and the effective thickness $t_{eff\,Ta}$. Guidelines have been added to this plot (dashed and dash–dot lines) to emphasize the increasing trend of the two data sets: it appears that without considering the effective thickness of the Ta ribbons ($t_{eff\,Ta}$) the size effect on the Cu/Ta hardness would clearly be overestimated. The hardness evolution plotted versus the theoretical diameter thus gives inaccurate information for the Cu/Ta system.

For samples a8–a12, the hardness of the Ta + Cu-0 zones increases from 4.5 to 5.2 GPa. Sample a13 corresponds to the hot extruded state. The hardness of this sample appears lower because of the high temperature of the extrusion stage (700 °C) that acts as a recrystallization heat treatment. Hence to interpret the evolution of H, we must take into account the size, the cold working state and the local composition of the indented zone.

To complete the study of these local properties, UTS data were obtained for Cu/Ta and Cu/Nb conductors at 293 K from classic tensile tests. In particular, the UTS for the Cu/13 vol.% Ta system reaches 634 MPa for a diameter of 2.41 mm (sample a9) and 711 MPa for a diameter down to 1.83 mm (sample a10) with an effective Ta thickness in the 24–820 nm range. For the Cu/11.7 vol.% Nb system, UTS reaches 576 MPa for a conductor diameter of 2 mm and a Nb fiber diameter of 830 nm. In both cases, these strengths deviate strongly from the classic ROM results

calculated considering fully cold worked bulk materials (σ_{UTS} (Cu) = 400 MPa, σ_{UTS} (Nb) = 1400 MPa and σ_{UTS} (Ta) = 1800 MPa): σ_{UTS} (ROM-Cu/13% Ta) = 586 MPa and σ_{UTS} (ROM-Cu/11.7% Nb) = 510 MPa.

5.3. Discussion: comparison with the Cu/Nb system

In Fig. 7(a), which shows the influence of the size parameter on the mechanical properties, different behaviors are noted:

- For $d_\alpha > 10$ μm, the hardness data for large Cu channels are higher than the literature hardness data for bulk coarse-grain Cu ($H_{\mu Cu} = 1.6$ GPa). This behavior may be a consequence of different effects: (i) the influence of pile-up around Cu indents that leads to an underestimation of the indenter contact area and thus to an overestimation of the hardness [15,27]; (ii) as observed in the TEM study, the larger Cu channels are nanostructured. Therefore, hardness data for large Cu channels tend toward hardness data for nanometre-sized Cu ($H_{nCu} = 2.2$ GPa).
- For smaller size ($d_\alpha < 10$ μm), we observed an increase of the hardness in the nanocomposite regions.

In a previous study of Cu/Nb multifilamentary conductors, a threshold was also observed at 10 μm, below which strengthening becomes important. This strengthening was shown to be linked to a restriction of the dislocation mobility by the microstructure dimension associated with impenetrable Cu/Nb interfaces [15]. These phenomena could be also responsible for the hardness evolution observed in the Cu/Ta multifilamentary conductors.

Fig. 8 illustrates the deviation of the hardness from the nano-ROM (n-ROM) values:

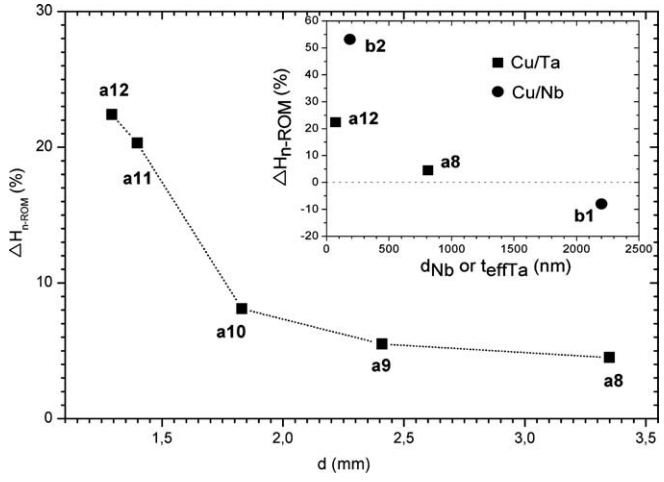

Fig. 8. Deviation $\Delta H_{n\text{-}ROM}$ (%) of the hardness H from the nanostructured material ROM hardness ($H_{n\text{-}ROM}$) versus the conductor diameter d for Cu/Ta conductors. The inset shows the deviation $\Delta H_{n\text{-}ROM}$ (%) of the hardness from $H_{n\text{-}ROM}$ versus d_{Nb} or t_{effTa} for Cu/Ta and Cu/Nb conductors.

$$\Delta H_{n\text{-}ROM} = (H - H_{n\text{-}ROM})/H_{n\text{-}ROM} \quad (1)$$

where $H_{n\text{-}ROM}$ is calculated using nanometer-sized material properties and local volume fractions of Cu, Ta or Nb (X_{nTa}, X_{nNb} and X_{nCu} in Table 3) as follows:

$$H_{n\text{-}ROM} = X_{nTa}H_{nTa} + X_{nCu}H_{nCu} \text{ or}$$
$$H_{n\text{-}ROM} = X_{nNb}H_{nNb} + X_{nCu}H_{nCu} \quad (2)$$

H_{nCu} corresponds to the literature data for nanometer-sized Cu given earlier. H_{nTa} was estimated from the Ta and Nb UTS values (σ_{UTS} (Nb) = 1400 MPa and σ_{UTS} (Ta) = 1800 MPa) by considering (following Tabor's law) that the ratio H_{nTa}/H_{nNb} is equal to σ_y (Ta)/σ_y (Nb), where σ_y are the yield stresses. Since in fully cold worked (nanostructured) bulk materials the UTS value is close to the yield stress, we can consider that $H_{nTa}/H_{nNb} \approx \sigma_{UTS}$ (Ta)/σ_{UTS} (Nb); with $H_{nNb} = 4.2$ GPa (literature data), this gives $H_{nTa} = 5.4$ GPa. This value must be compared to the literature data for nanostructured bulk Ta. To the authors' knowledge no data are available for such a system. Data can be found for Ta thin films [28,29], where either the substrate affects the nanohardness experiments (at large penetration depth) or a possible indentation size effect can affect the data (at small penetration depth): a hardness of 11 GPa has been reported in these cases. It is also possible to find data for severely deformed Ta, via the equal-channel angular extrusion process, that exhibits a microhardness value of 220 HV [30]. This very low value can be explained by the fact that after a "rather small" true strain of 5, Ta is not already nanostructured but still contains micrometer-sized grains containing dislocation cells, which cannot be considered as true nanograins. Thus, we consider our estimation $H_{nTa} = 5.4$ GPa as a plausible value.

For Cu/Ta wires, $\Delta H_{n\text{-}ROM}$ is plotted versus the conductor diameter d in Fig. 8: its value is always positive and increases as the dimension decreases during the drawing process. This positive deviation from the n-ROM prediction shows that the strength of the Cu/Ta nanocomposite zones is greater than a simple combination of individual nanostructured Cu and Ta phases. One needs to remember here that these nanostructured phases already exhibit some strengthening due to their microstructural dimensions that induce changes in the plasticity mechanisms such as dislocation starvation (reduced full dislocation nucleation, partial dislocation nucleation, mobility restriction) or grain boundary sliding. Thus the positive value of $\Delta H_{n\text{-}ROM}$ shows that beside the size effect induced by the nanostructuring of each individual phase there are extra strengthening mechanisms when reducing microstructure size. Among the additional effects is the role of Cu/Ta interfaces. In the Cu/Nb system, they are observed to be barriers to the motion of dislocations [13,15]: similarly, it can be assumed that the Cu/Ta interfaces are sinks to dislocations. Another effect may be the influence of each phase's geometry on the plasticity mechanisms, such as in whiskers considered as one-dimensional systems. To compare this "extra" strengthening in Cu/Ta

and Cu/Nb systems, $\Delta H_{\text{n-ROM}}$ is plotted versus $t_{\text{eff Ta}}$ and d_{Nb} (inset in Fig. 8). The Cu/Ta samples, at nanometer scales, exhibit lower deviation from n-ROM prediction than Cu/Nb samples where Nb filaments, which are nanowhiskers, are responsible for a strong strengthening effect. This unexpected result is probably due to the distorted two-dimensional ribbon morphology of the Ta filaments that prevents one from considering them as one-dimensional whiskers: the consequence is a lower local strengthening of Cu/Ta conductors. The same trend is observed when interpreting the UTS data. The UTS for sample a10 seems to deviate from the ROM value more strongly (+22.2%) than that for the Cu/Nb conductor (+11.4%) with similar theoretical dimensions ($d_{\text{Ta}} = 810$ nm; $d_{\text{Nb}} = 830$ nm). However, if one takes into account the true size of the Ta ribbons ($24\text{ nm} < t_{\text{eff Ta}} < 820$ nm) the deviation from ROM appears smaller. The apparent good properties of the Cu/Ta system are mainly due to the early refinement of the structure with the curling phenomenon. Moreover, Ta ribbon thickness saturation in very fine wires can also limit the mechanical properties. This size stabilization is probably linked to a deformation restriction caused by the high Ta hardness and by the tangles between Ta filaments.

Therefore, the positive value $\Delta H_{\text{n-ROM}}$ shows that the decrease of the dimensions in Cu/Ta nanocomposite zones leads to an increase of hardness which is mainly due to the coupling between "traditional" size effects (dislocation starvation) in individual phases and fcc/bcc interface effects. However, extra strengthening resulting from the geometry of the reinforcing filaments (ribbons versus cylindrical fibers) appears weak or nonexistent. Meanwhile the large Cu channels exhibit rather weak strengthening. As a consequence, these conductors present a complex plasticity distribution: in order to understand the mechanisms of elastic and plastic deformation of the multiscale Cu matrix and the Ta nanoribbons, neutron scattering experiments with in situ deformation are in progress. This will also help us to measure the stress level at the formation of internal fractures and link these data to the occurrence of internal defects that have prevented, so far, the fabrication of Cu/Ta conductors with diameters smaller than 1.3 mm at 85^3 filament stage. Indeed, the very fine high-strength wires suffer from periodical core fractures, called "central bursting", during hot extrusion and cold drawing at the stages 85^3 and 85^4 filaments [31]. It is worth mentioning that these defects are also observed during the drawing of Cu/Ta "in situ" composites [19].

6. Conclusion

Cu/Ta nanofilamentary wires obtained by SPD applied via successive hot extrusion and cold drawing steps were characterized and compared to Cu/Nb conductors. During the fabrication process, a very fine microstructure is achieved in the Cu/Ta wires:

- The Cu microstructure appears similar to that observed in Cu/Nb wires: (i) the largest Cu channels correspond to heavily deformed Cu composed of grains in the micrometer and nanometer range with a high dislocation density; (ii) the finest Cu channels are composed of single grains elongated along the drawing axis.
- XRD studies revealed the presence, in Cu, of a major $\langle 1\,1\,1\rangle$ texture component with a non-negligible remnant $\langle 2\,0\,0\rangle$ component which was not observed in Cu/Nb conductors and seems to be associated with recrystallization mechanisms during annealing and hot extrusion steps.
- The Ta filaments develop, like Nb, a strong $\langle 1\,1\,0\rangle$ texture.
- TEM studies revealed the development, during drawing steps, of a strong curled structure characterized by the flattening and the interfolding of Ta filaments that become ribbons despite the fact that they were initially cylindrical. This "curling" phenomenon, leading to a very fine microstructure, is not observed in "continuous" Cu/Nb conductors: Nb filaments retain a cylindrical shape and are considered as nanowhiskers.

The difference in microstructural evolution observed in Cu/Nb and Cu/Ta systems during SPD leads to different mechanical behavior: Cu/Ta composites show greater UTS at comparable drawing ratio, which is the result of the intrinsic beneficial mechanical properties of Ta and of an early refinement of the microstructure through the curling phenomenon. Nevertheless, the local study carried out by nanoindentation reveals, in highly drawn Cu/Ta wires, a lower deviation from ROM predictions probably also resulting from the Ta microstructure evolution. Indeed, due to their curled flattened morphology, Ta ribbons do not behave as whiskers as observed in Cu/Nb nanofilamentary wires, where the whisker effect plays an important role in the high strength obtained.

Furthermore, after high drawing strains, it was shown that the Ta ribbon thickness tends to saturation around 20 nm, which is probably a limitation to further plastic co-deformation of the distorted nanocomposite zones containing the Ta fibers; further reduction of the wire can result in fracture of the ribbons. Thus, it appears difficult to obtain very fine ultrahigh-strength Cu/Ta conductors as the strengthening by size reduction through cold drawing is limited: the Cu/Ta system becomes too hard to deform and periodical internal fractures occur. In Cu/Nb composites such saturation in the dimension of the fibers was not observed; therefore, a larger drawing ratio is assumed to be attainable for the Cu/Nb system without the occurrence of central bursting.

From the electrical point of view, the resistivity of the Cu/Ta conductors remains close to 0.4 $\mu\Omega$ cm at 77 K and therefore satisfies the high-conductivity requirement for magnet applications.

It was shown previously that, during SPD, the reinforcing phase transforms into one-dimensional geometry

(whiskers) in nanofilamentary Cu/Nb wires; to improve the mechanical properties Ta was chosen to replace Nb because of the higher shear modulus supposed to enhance the whisker effect. However, the large shear modulus difference between Ta and Cu induces higher deformation incompatibility during SPD, leading the reinforcing phase to transform into a less efficient two-dimensional geometry (ribbons). The Cu/Ta system is therefore not as efficient as the Cu/Nb system for the high-strength requirements for magnet applications.

Finally, the choice of bcc metal to reinforce the Cu matrix is crucial to attain ultrahigh strength. It appears necessary to consider carefully the combination of material properties at the microscopic scale to obtain a controlled microstructure and an efficient strengthening of nanofilamentary composites. In other words, size and also geometry play key roles in the plasticity of nanomaterials.

Acknowledgements

The authors thank the technical team of LNCMP, L. Bendichou, G. Coffe, N. Ferreira, J.M. Lagarrigue and J.P. Laurent, who participated in the fabrication of the conductors.

References

[1] Spencer K, Lecouturier F, Thilly L, Embury JD. Adv Eng Mater 2004;6(5):290.
[2] Bevk J, Harbison JP, Bell JL. J Appl Phys 1978;49(12):6031.
[3] Funkenbusch PD, Courtney TH. Scripta Metall 1989;23:1719.
[4] Spitzig WA, Pelton AR, Laabs FC. Acta Metall 1987;35(10):2427.
[5] Gil Sevillano J. J Phys III 1991;1:967.
[6] Pourrahimi S, Nayeb-Hashemi H, Foner S. Metall Trans A 1992;23A:573.
[7] Raabe D, Heringhaus F, Hangen U, Gottstein G. Z Metallkd 1995;86(6):405.
[8] Raabe D, Heringhaus F, Hangen U, Gottstein G. Z Metallkd 1995;86(6):416.
[9] Popova EN, Popov VV, Rodionova LA, Romanov EP, Sudareva SV, Hlebova NE, et al. Scripta Mater 2002;46:193.
[10] Popova EN, Popov VV, Romanov EP, Hlebova NE, Shikov AK. Scripta Mater 2004;51:727.
[11] Hong SI, Hill MA. Scripta Mater 2001;44:2509.
[12] Pantsyrnyi V, Shikov A, Vorobieva A, Khlebova N, Potapenko I, Silaev A, et al. IEEE Trans Appl Supercond 2000;10(1):1263.
[13] Thilly L, Ludwig O, Véron M, Lecouturier F, Peyrade JP, Askénazy S. Philos Mag A 2002;82(5):925.
[14] Dupouy F. Doctoral Thesis, INSA, France; 1995.
[15] Thilly L, Lecouturier F, Von Stebut J. Acta Mater 2002;50(20):5049.
[16] Thilly L. Doctoral Thesis, INSA, France; 2000.
[17] Dupouy F, Askénazy S, Peyrade JP, Legat D. Mech Compos Mater 1995;31(4):518.
[18] Krotz PD, Spitzig WA, Laabs FC. Mater Sci Eng 1989;A110:37.
[19] Spitzig WA, Krotz PD. Acta Metall 1988;36(7):1709.
[20] Biselli C, Morris DG. Acta Mater 1996;44(2):493.
[21] Sauvage X, Wetscher F, Pareige P. Acta Mater 2005;53:2127.
[22] Thilly L, Colin J, Lecouturier F, Peyrade JP, Grilhé J, Askénazy S. Acta Mater 1999;47(3):853.
[23] Thilly L, Lecouturier F, Véron M, Snoeck E, Peyrade JP, Askénazy S. J Phys IV France 2001;11:33.
[24] Hosford Jr WF. Trans Metall Soc AIME 1964;230:12.
[25] Dupouy F, Snoeck E, Casanove MJ, Roucau C, Peyrade JP, Askénazy S. Scripta Mater 1996;34(7):1067.
[26] Kraft FF, Chakkingal U, Baker G, Wright RN. J Mater Process Technol 1996;60:171.
[27] Oliver WC, Pharr GM. J Mater Res 1992;7:6.
[28] Saha R, Barnard JA. J Cryst Growth 1997;174:495.
[29] Nguyen TD, Barbee Jr TW. Mater Res Soc Symp Proc 1998;522:269.
[30] Sandim HRZ, McQueen HJ, Blum W. Scripta Mater 2000;42:151.
[31] Vidal V, Thilly L, Lecouturier F. Mater Sci Forum 2006;503–504:639.